Biosensors and Bioelectronics 142 (2019) 111512

Contents lists available at ScienceDirect

Biosensors and Bioelectronics

journal homepage: www.elsevier.com/locate/bios

Bionanoelectronic platform with a lipid bilayer/CVD-grown MoS_2 hybrid

Yunjeong Park[a,1], Byunggil Kang[b,1], Cheol Hyoun Ahn[c], Hyung Koun Cho[c], Hyukjoon Kwon[b], Sungsu Park[a], Junhwan Kwon[d], Myunghwan Choi[d], Changgu Lee[a,b,**], Kyunghoon Kim[a,*]

[a] School of Mechanical Engineering, Sungkyunkwan University (SKKU), Suwon 16419, Republic of Korea
[b] SKKU Advanced Institute of Nanotechnology (SAINT), Sungkyunkwan University (SKKU), Suwon 16419, Republic of Korea
[c] School of Advanced Materials Science and Engineering, Sungkyunkwan University (SKKU), Suwon 16419, Republic of Korea
[d] Department of Biomedical Engineering, Sungkyunkwan University (SKKU), Suwon 16419, Republic of Korea

ARTICLE INFO

Keywords:
MoS_2
Lipid bilayers
Field effect transistors
Gramicidin A

ABSTRACT

We demonstrate a bionanoelectronic platform for a supported lipid bilayer formed on an MoS_2 film for biosensing, biomolecule recognition, and bioelectronic applications. A large-area MoS_2 film was synthesized on a sapphire substrate and treated with O_2 plasma or Al_2O_3 deposition to change the surface from hydrophobic to hydrophilic. Measurements of fluorescence and fluorescence recovery after photobleaching confirmed the physical properties of the lipid bilayer on the treated surfaces. We fabricated an electronic device using the treated MoS_2 film and characterized the influence of the lipid bilayer on its electrical properties. Furthermore, transmembrane ion channels peptide (gramicidin A) were incorporated into the lipid bilayer and modulations of the electrical properties of the device under various pH conditions and calcium ion were observed. This sensitive and stable platform has strong potential for housing artificial channels and transmembrane ion channels for advanced bioapplications.

1. Introduction

Biological systems are responsible for complicated functions and diverse interactions such as signal transmission, data transduction, energy synthesis, and organism reproduction(Albert et al., 2007). Biological information is delivered across cell membranes by proton pumps, ion channels, ion gradients, electrical signals, and biomolecules. Compared with the mechanism of information processing in nature, that in man-made devices is much less sophisticated, which poses challenges related to miniaturization, finite reaction rates and other problems(Noy, 2011).

Nevertheless, researchers have extensively investigated artificial biological systems using nanomaterials to produce next-generation devices. One-dimensional (1D) nanomaterials, such as nanowires and nanotubes, have been reported as transducing materials for the study of biomolecules and biosystems on the basis of their size compatibility with biomolecules and their chemical inertness.

Bioapplications of 1D materials have shown that ultrasensitive and nanoscale devices are comparable to biomolecules(Kim et al., 2016; Yin et al., 2018). However, 1D materials have limitations with respect to synthesis, device fabrication, and mass production because their thickness, purities, defect concentrations, and chiralities are uncontrollable. Additionally, surface roughness causes noise because of curvature, which makes using 1D-material-based devices for biosensors or bioelectronics difficult(Go et al., 2012).

Two-dimensional (2D) materials have shown strong potential as transducing materials for sensing biomolecules and bioapplications because of their low noise, good scalability, ultra-sensitivity, and good compatibility with biomaterials(Sarkar et al., 2014; Zhang et al., 2017; Kireev and Offenhausser, 2018; Jiang et al., 2019). MoS_2, a representative 2D transition-metal dichalcogenide, has been studied for its usage in biosensors such as pH sensors, DNA hybridization detection, and protein sensors with antibodies(Lee et al., 2015; Qiao et al., 2018; Kaushik et al., 2019). Unlike graphene with the zero bandgap, the sizable bandgap of MoS_2 overcomes the key drawbacks of graphene for electronic devices and MoS_2–based field-effect transistor (FET) offers superior sensitivity in biosensing applications for specific detection of biomolecules (Sarkar et al., 2014). MoS_2, which has no dangling bonds at the basal surface and is stable in both water and oxygen media, can be used with a lipid bilayer that can accommodate artificial channels, proton pumps, and proteins that transmit biological signals in and out of cells (Dalila R et al., 2019; Zhao and Dai, 2015). Thus, a hybrid

* Corresponding author.
** Corresponding author. School of Mechanical Engineering, Sungkyunkwan University (SKKU), Suwon 16419, Republic of Korea.
E-mail addresses: peterlee@skku.edu (C. Lee), kenkim@skku.edu (K. Kim).
[1] These authors contributed equally to this work.

https://doi.org/10.1016/j.bios.2019.111512
Received 23 April 2019; Received in revised form 20 June 2019; Accepted 12 July 2019
Available online 17 July 2019
0956-5663/

structure comprising a lipid bilayer and MoS_2 could provide a new biomimetic platform for bridging the gap between biology and electronics..

Herein, a bioelectronic platform with a supported lipid bilayer (SLB) and synthesized MoS_2 is demonstrated for a scalable, reliable, and low-cost biological toolkit. First, we synthesized MoS_2 films via chemical vapor deposition (CVD) and characterized them by atomic force microscopy (AFM), X-ray photoelectron spectroscopy (XPS), and Raman spectroscopy. We formed the SLB via a vesicle fusion method on a hydrophilic MoS_2 film modified by treatment with O_2 plasma or Al_2O_3 deposition. Subsequently, we performed fluorescence measurements and fluorescence recovery after photobleaching (FRAP) tests to characterize the SLB. MoS_2-FETs were fabricated and covered by an SLB that housed proton channels of a transmembrane peptide (gramicidin A). The MoS_2 FETs detected the number of protons in a buffer solution and changed the electrical properties of the solution under diverse pH conditions, depending on the presence or absence of the SLB, gramicidin A and calcium ion in the solution.

2. Experimental

2.1. Synthesis of MoS_2

A 10.5 mm × 10.5 mm sapphire substrate, molybdenum (VI) oxide (MoO_3), and sulfur (S) powder were prepared for MoS_2 thin-film growth. A quartz boat that contained 2 mg of MoO_3 powder and sapphire was placed in the center of the furnace of a CVD system. Then, 30 mg of S powder was placed on the edge of the furnace near the gas outlet. The furnace was heated to 300 °C with the sample chamber under argon (Ar) gas flowing at 200 sccm, and these conditions were maintained for 10 min. The furnace was then heated to 700 °C with Ar gas flowing at 20 sccm, and these conditions were maintained for 10 min for growth of the MoS_2 film. Subsequently, the CVD system was rapidly cooled to room temperature.

2.2. Surface engineering and characterization of the MoS_2 film

The MoS_2 surface was treated with O_2 plasma, which is a physical treatment, using the inductively coupled plasma (ICP) mode (SNTEK). The MoS_2 film was treated with plasma for 5 s at a power of 60 W and an O_2 gas flow rate of 30 sccm. In a separate experiment, a 30-nm-thick Al_2O_3 dielectric layer was deposited onto the MoS_2 surface via atomic layer deposition (ALD).

A droplet analyzer (SDL200TEDZD) was used to measure the direct contact angle, and ~1 μL of deionized (DI) water was dropped onto the surfaces. The contact angle measurement was conducted at room temperature and at 5–6% relative humidity.

2.3. Formation of the biomimetic membrane on the MoS_2 film and incorporation of gramicidin A

Chloroform solutions of 1,2-dioleoyl-*sn*-glycero-3-phosphocholine (DOPC) and 1,2-dioleoyl-*sn*-glycero-3-phosphoethanolamine-*N*-(lissamine rhodamine B sulfonyl) ammonium salt (Rho-PE) were prepared by Avanti Polar Lipids. DOPC was mixed with Rho-PE at a concentration of 0.01% in a glass vial. The mixture was then dried with N_2 gas until a thin film was formed under vacuum for 1 h. The dry lipid was rehydrated at a concentration of 1 mg/mL in 10 mM phosphate-buffered saline (PBS). The suspension was treated with the freeze–thaw method to produce unilamellar vesicles and was extruded in a 200-nm polycarbonate filter to obtain uniformly sized vesicles. The surface-treated MoS_2 was incubated in the suspension for 30 min at room temperature. The remaining vesicles in the suspension were removed by washing with PBS. Gramicidin A (Sigma-Aldrich) was mixed at a molar ratio of 100:1 before solvent evaporation followed by SLB preparation.

Fluorescence microscopy with an oil immersion lens (TE2000-U, Nikon) was used to produce the fluorescence images.

The FRAP test was conducted using a multiphoton fluorescence microscope (Leica TCS SP8 with a water immersion objective lens). The fluorophores were excited by a 514-nm laser that was controlled with the PrairieView software. Fluorophores were bleached for 10 s, and the recovery process was imaged every 5 s.

2.4. Fabrication and analysis of the lipid bilayer-coated MoS_2 bioelectronic device

We fabricated water-gated MoS_2 FET arrays. The FETs were patterned by photolithography and e-beam evaporation. After lift-off, the substrate was coated with a photoresist to create an open channel formed by the SLB. We developed a 2-μm^2 area within the MoS_2 channel and installed the channel for polydimethylsiloxane (PDMS) as a reservoir. A reference electrode was used to apply an electric field to the channel. The electrical performance of the MoS_2 FETs was measured with a probe station system (MS TECH 4000, Keithley) at room temperature. The device response in the pH solution as measured at a 0.1-V source–drain voltage. The buffer exchange in the PDMS reservoir was limited by the maximum syringe pump flow rate of 500 μL/min.

3. Results and discussion

3.1. Synthesis of MoS_2

Fig. 1A shows a schematic of the MoS_2 synthesis process in the CVD system, where MoO_3 and S powders were used as precursors. When the temperature increases to 700 °C, the rich sulfur vapor reduces the MoO_3 powder to suboxide MoO_{3-x}, which is susceptible to sulfurization (Lee et al., 2012; Zhang et al., 2015). These compounds spread out over the substrate gradually to form the MoS_2 film at atmospheric pressure using high-purity Ar as the transport gas. Moreover, to synthesize a high-quality MoS_2 film, we used a sapphire substrate for epitaxial growth (Dumcenco et al., 2015). As a result, the synthesized MoS_2 film on sapphire shows some color contrast compared with the bare sapphire substrate, as shown in Fig. 1B. The thickness of the MoS_2 film was determined by AFM (Fig. 1C). The height of the edge of the MoS_2 film was 19 nm, which corresponds to approximately 25 MoS_2 layers.

We next used Raman spectroscopy to examine the quality of the prepared MoS_2 films. The Raman spectrum of MoS_2 features two prominent peaks: the E^1_{2g} mode corresponding to S and Mo atoms oscillating in the antiphase parallel to the crystal plane and the A_{1g} mode corresponding to S atoms oscillating in the antiphase out of the plane (Li et al., 2012). In Fig. 1D, the peaks for the E^1_{2g} (383.1 cm^{-1}) and A_{1g} (408.1 cm^{-1}) modes have a peak distance of $\Delta k \approx 25\ cm^{-1}$, which indicates that the grown material is a multilayer film. Raman spectra collected across the MoS_2 film confirmed the quality of the film and the possibility of mass producing the electronic platform.

3.2. Surface modified MoS_2 analysis

Fig. 2 shows the difference between the wetting properties of the surfaces of bare and treated MoS_2 films. Because the head section of the lipid is hydrophilic, it tends to be unstable on the hydrophobic MoS_2 surface. Consequently, modifying the MoS_2 surface was essential before creating the hybrid structure. We used O_2 plasma treatment and Al_2O_3 deposition for surface modification. To confirm the surface energy, we measured the static contact angle of water droplets on the MoS_2 films to indirectly show the wetting properties of their surface.

As shown in Fig. 2A–C, the surface of the as-prepared films was modified; the contact angle shifted from 89° to 51–58° after the treatments, which transformed the surface from hydrophobic to hydrophilic. Furthermore, as the power of the plasma was increased from 0 to 100 W in 20 W increments, the contact angle of the as-grown MoS_2 decreased (SI, Fig. S1). This decrease of the contact angle indicates that, with

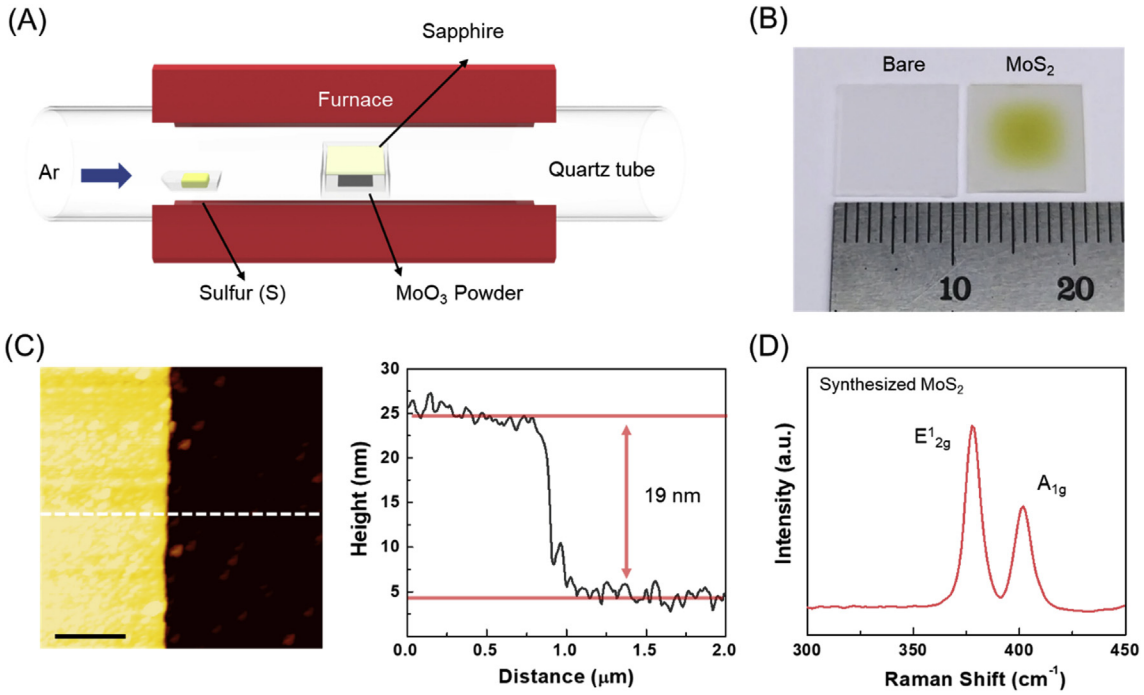

Fig. 1. Synthesis and characterization of the large-area MoS_2. (A) Schematic of the chemical vapor deposition approach for MoS_2 synthesis. (B) Photograph of a centimeter-scale multilayer MoS_2 film grown on sapphire. (C) Left: AFM image of the multilayer MoS_2 film. The scale bar is 1 μm. Right: thickness profile along the line in the AFM image. (D) Raman spectrum of the multilayer MoS_2 film on sapphire. The laser excitation wavelength was 405 nm.

increasing plasma power, the free energy that determines the extent of the interaction between the water and the MoS_2 film surface increased. On the basis of the magnitude of the contact angle and the integrity of the MoS_2 structure, we selected the film treated at 60 W of plasma power for further characterization.

To characterize the MoS_2 quality after the plasma treatment, we used Raman spectroscopy and XPS to characterize the sample before and after the treatment under 60 W plasma. The equivalence of the Raman peaks in positions corresponding to the E^1_{2g} and A_{1g} peaks between bare MoS_2 (black curve) and O_2 plasma-treated MoS_2 (red curve) indicates that the plasma treatment did not influence the Raman peaks, as shown in Fig. 2D. Because the as-grown MoS_2 film was thick (19 nm), the damage to the surface from the O_2 plasma (60 W, 5 s) occurred only within a few top layers of MoS_2.

To elucidate the change in chemical composition of the surface of the MoS_2 film, XPS analysis was conducted before and after the 60 W plasma treatment; the results are shown in Fig. 2E. The XPS survey spectrum of the bare MoS_2 shows three dominant peaks at 226.9 eV,

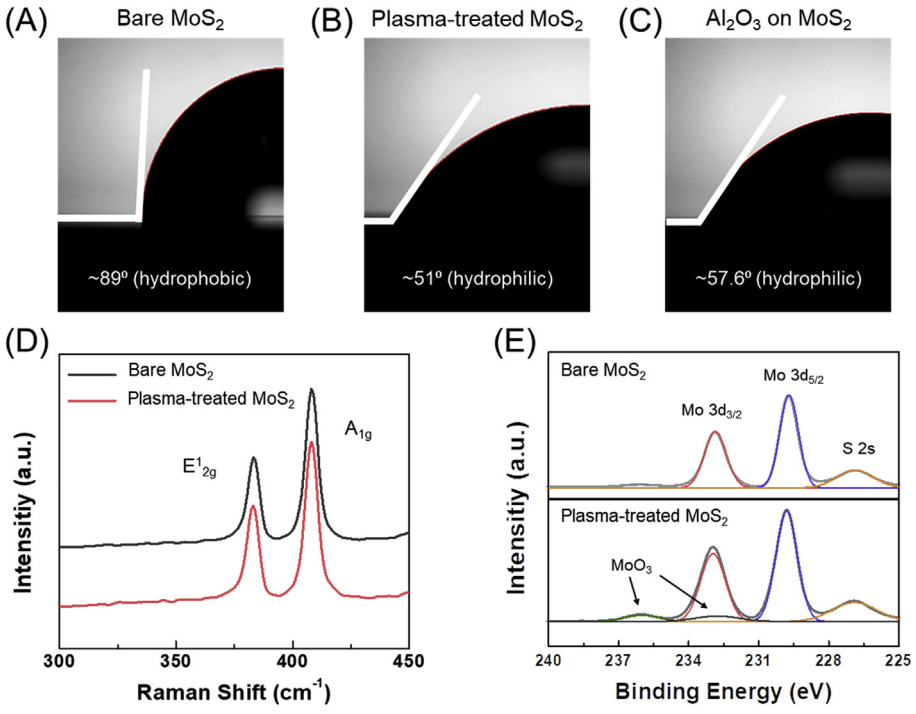

Fig. 2. Surface characterization of modified MoS_2. Water contact angles of (A) an as-grown MoS_2 film, (B) a plasma-treated MoS_2 film, and (C) an MoS_2 film with deposited Al_2O_3. (D) Raman spectra of the as-grown and the plasma-treated MoS_2 films. The laser excitation wavelength was 405 nm. (E) XPS spectra of Mo 3d and S 2s binding energies for as-grown (upper) and plasma-treated MoS_2 films (lower).

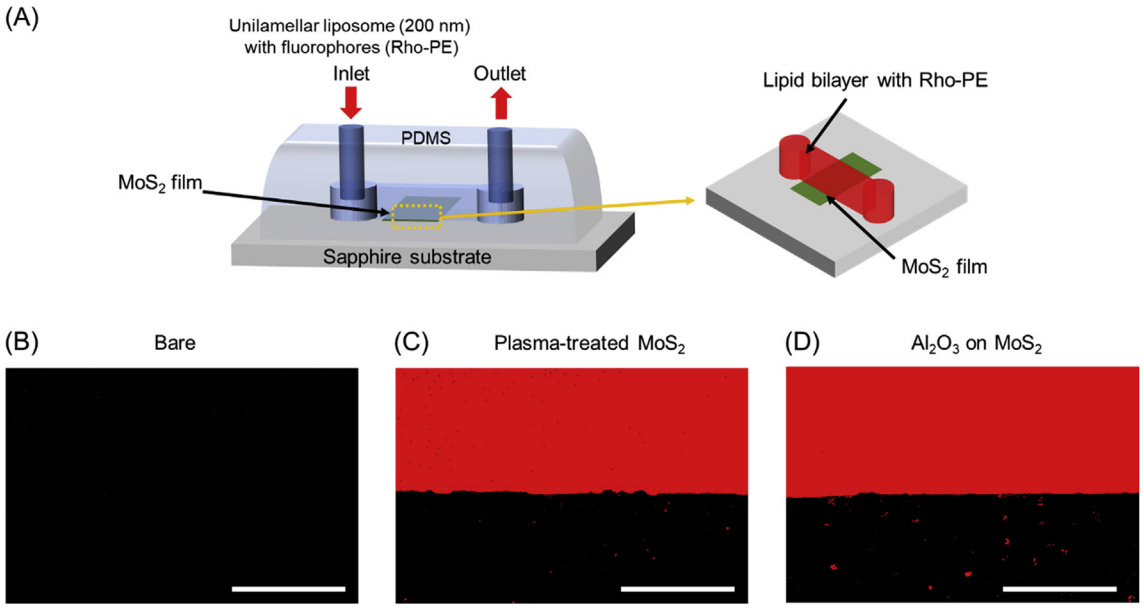

Fig. 3. Schematic of lipid bilayer formation and fluorescent images of the fluorescein (Rho PE)-labeled lipid bilayer on MoS_2. (A) Schematic of the PDMS microfluidic channel for lipid bilayer formation on a MoS_2 film. Unilamellar vesicles of the DOPC lipid are fused onto MoS_2 on the sapphire substrate. (B) No lipid bilayer formation was observed on an as-grown MoS_2 film (dark region). (C,D) Lipid bilayer formation was observed on plasma-treated and Al_2O_3-deposited MoS_2 films (red region). The scale bar is 20 μm. (For interpretation of the references to color in this figure legend, the reader is referred to the Web version of this article.)

229.8 eV, and 232.9 eV, which denote the binding energies of S 2s, Mo $3d_{5/2}$, and Mo $3d_{3/2}$, respectively (Islam et al., 2014; Chow et al., 2015). However, the O_2 plasma treatment of the MoS_2 film generated an additional peak at 236.08 eV by forming Mo–O bonds, which indicates the presence of Mo in its higher oxidation state of Mo^{6+} (Islam et al., 2014; Chow et al., 2015). As particles with a high energy bombard the MoS_2 surface, they create S vacancies because the mass of S is smaller than that of Mo. Therefore, the defect area can be oxidized in an oxygen-containing environment. The oxidation process on the surface can be expressed as $2MoS_2 + 7O_2 \rightarrow 2MoO_3 + 4SO_2$ (Islam et al., 2014; Chow et al., 2015). The top few layers of MoS_2 were oxidized under appropriate O_2 plasma conditions while the underlying layers remained intact, as monitored through measurements of the electrical properties of the MoS_2 film. After the plasma treatment, the SLB was successfully formed on the MoS_2 surface because MoO_3 is hydrophilic.

3.3. Fomation of lipid bilayer on MoS_2 film

Fig. 3A shows a schematic of the lipid bilayer platform on the MoS_2 film with the vesicle. The vesicle suspension was prepared with dried DOPC film and mixed with Rho-PE for fluorescence imaging. The 200-nm-sized unilamellar vesicles were prepared by the conventional freeze–thaw and extrusion method. The PDMS that was patterned with a microfluidic channel was mounted onto the MoS_2 film. The syringe pump injected the lipid suspension slowly, and the film was incubated for 3 h to form the lipid bilayer on the MoS_2 surface via the vesicle fusion method (Artyukhin et al., 2005; Chen et al., 2019). The vesicle was ruptured on the MoS_2 surface and converted into a planar lipid bilayer via self-assembly. Fig. 3B–D shows fluorescence images recorded after formation of the lipid bilayer. The black region in the fluorescence image in Fig. 3B is due to the absence of the SLB with the fluorophore on untreated MoS_2; the red regions in Fig. 3C and D indicate the SLB on the MoS_2 areas subjected to O_2 plasma treatment and Al_2O_3 deposition, respectively.

A FRAP test was conducted to verify the fluidity and mobility of the lipid molecules. FRAP is a widely used approach to measure the lateral mobility of lipid membranes formed on a substrate. Kang et al. published a brief equation for calculating the diffusion coefficient from FRAP data (Kang et al., 2012, 2015). They calculated the diffusion coefficient at one-half of the recovery time and the effective radius (r_e) in a circular region of interest. The effective radius was obtained from the nominalized post-bleach profile using the half-width at a total height (K) of 0.86 (SI, Fig. S2). The effective radius was slightly larger than the nominal radius because the fluorophore-tagged lipid diffused during bleaching. The equation for the diffusion coefficient (D_{plasma}) is

$$D_{plasma} = \frac{r_e^2 + r_n^2}{T_{1/2}}$$

where $T_{1/2}$ is the half-time to recovery, r_e is the effective radius, and r_n is the nominal radius (Kang et al., 2012). Fig. 4A and C shows images of the fluorescence during the recovery process. The fluorescence intensity of the lipid bilayer recovered by 50–80% in 240 s compared with the pre-bleaching intensity (Fig. 4B and D). The fluorescence intensities at two independent bleaching spots are shown in the insets of Fig. 4B and D; the fluorescence intensity of both films recovered after 7–13 min.

The lipid bilayers showed high mobility; the in-plane lipid molecule diffusion coefficient in the plasma-treated sample (D_{plasma}) measured by FRAP was 1.53 $\mu m^2/s$ within 10% error according to the equation. The diffusion coefficient (D_{Al2O3}) of the lipid bilayer on Al_2O_3 was 3.75 $\mu m^2/s$. These results indicate that lipid molecules exhibit good continuity and fluidity on MoS_2, creating a biomimetic environment.

3.4. Bioelectronic platform analysis

To integrate the bioelectronics platform, we fabricated MoS_2 FET arrays on sapphire substrates by photolithography and e-beam metal evaporation with 5-nm-thick Cr and 50-nm-thick Au electrodes. To operate the device in the water phase, the source and drain electrodes were encapsulated with 30-nm-thick Al_2O_3 to prevent a short circuit due to the electric bias, as shown in the insets of Fig. 5A and B, respectively (Mao et al., 2017). The open channel of the passivated device was then treated with O_2 plasma to alter the surface energy. A PDMS reservoir was constructed to contain the buffer solution, which prevented the SLB from aggregating. The SLB was formed on the surfaces of both the plasma-treated and Al_2O_3-encapsulated MoS_2 films. An Ag/AgCl reference electrode was installed in the buffer solution as a top-

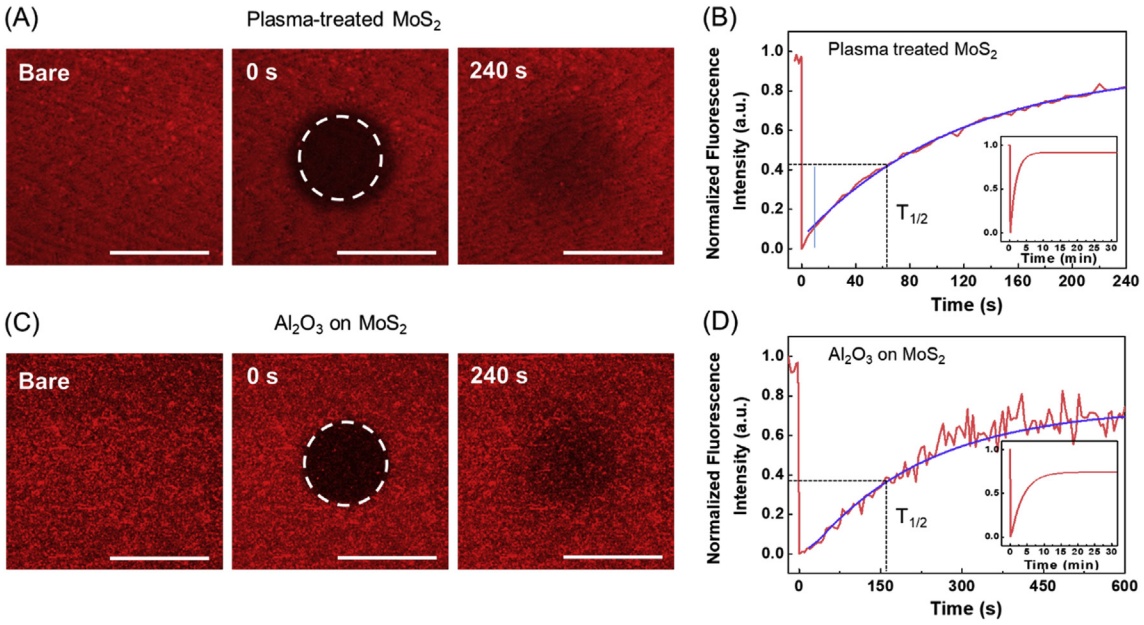

Fig. 4. FRAP tests for DOPC SLB with Rho-PE formed on modified MoS_2. (A,C) Representative pre- and post-bleaching and recovery fluorescence images of the plasma-treated and Al_2O_3-deposited MoS_2 films. The circular dashed line represents the user-defined bleaching spot with a 25-μm radius. The scale bar is 50 μm. (B,D) Plot of fluorescence intensity vs. time within the nominal bleaching region of interest. Inset: same data and fit for the full 30-min measurement.

gate voltage supplier.

The transfer curves of both devices showed n-type transistor behavior under two conditions—without the SLB and with the SLB—as shown in Fig. 5A and B. The drain current of both devices decreased after SLB deposition when the water top-gate voltage was increased because of charge trapping and screening of the electric field by the SLB. In previous studies, a lipid-bilayer-coated nanowire and nanotube p-type transistor showed a comparable current decrease because of the influence of the SLB (Misra et al., 2009; Tunuguntla et al., 2015; Chen et al., 2019). Moreover, the Dirac point of a graphene transistor after SLB deposition was positively shifted following a lower current in the electron regime of the transfer curve than that of the bare graphene device (Ang et al., 2010).

The MoS_2 FET with deposited Al_2O_3 exhibited better sensitivity and stability than the bare plasma-treated FET with an open channel under pH 4, 7, and 10 solutions, as shown in SI, Fig. S3. The accumulation of protons on the top surfaces of both device channels by the positive electric field changed the surface charge and enhanced the electrical performance (Sarkar et al., 2014). Hence, the dielectric material improved not only pH sensing via protonation between protons and the functional groups ($OH + H^+ \rightleftharpoons OH_2^+$) but also the stability by functioning as a passivation layer (Sarkar et al., 2014).

Hence, the hybrid structure of SLB on Al_2O_3-encapsulated MoS_2 in Fig. 6A was utilized as a bioelectronic platform to detect selective ions through insertion of the transmembrane peptide channel like a cell membrane. The Al_2O_3-encapsulated MoS_2 FETs without the SLB (black line) showed the same trend of pH sensing as that previously observed[8], whereas the device with SLB (red line) exhibited a constant current because of screening of the interaction between the proton and the device surface, as shown in Fig. 6B and C. The SLB on the device was subsequently incorporated with the transmembrane channel, gramicidin A, which transports protons. Gramicidin A serves as a passageway

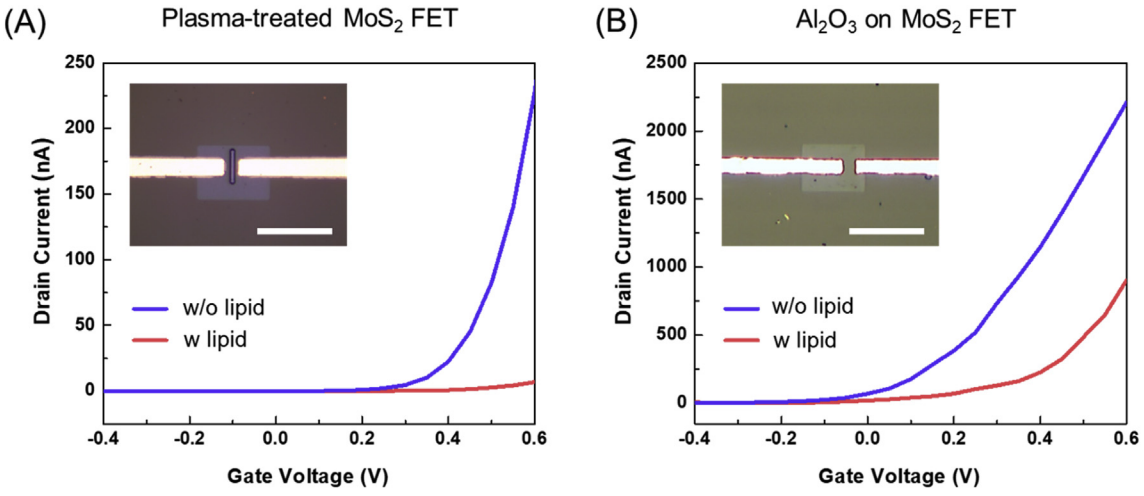

Fig. 5. Effect of lipid bilayers on device characteristics. Transfer characteristics of an uncoated MoS_2 device (blue lines) and lipid-bilayer-coated MoS_2 devices (red lines) after (A) plasma treatment of and (B) Al_2O_3 deposition onto the MoS_2 FET devices. The insets show optical microscope images of the device chip (A) passivated with a photoresist and (B) after deposition of Al_2O_3 onto the MoS_2 film. The scale bars are 20 μm. (For interpretation of the references to color in this figure legend, the reader is referred to the Web version of this article.)

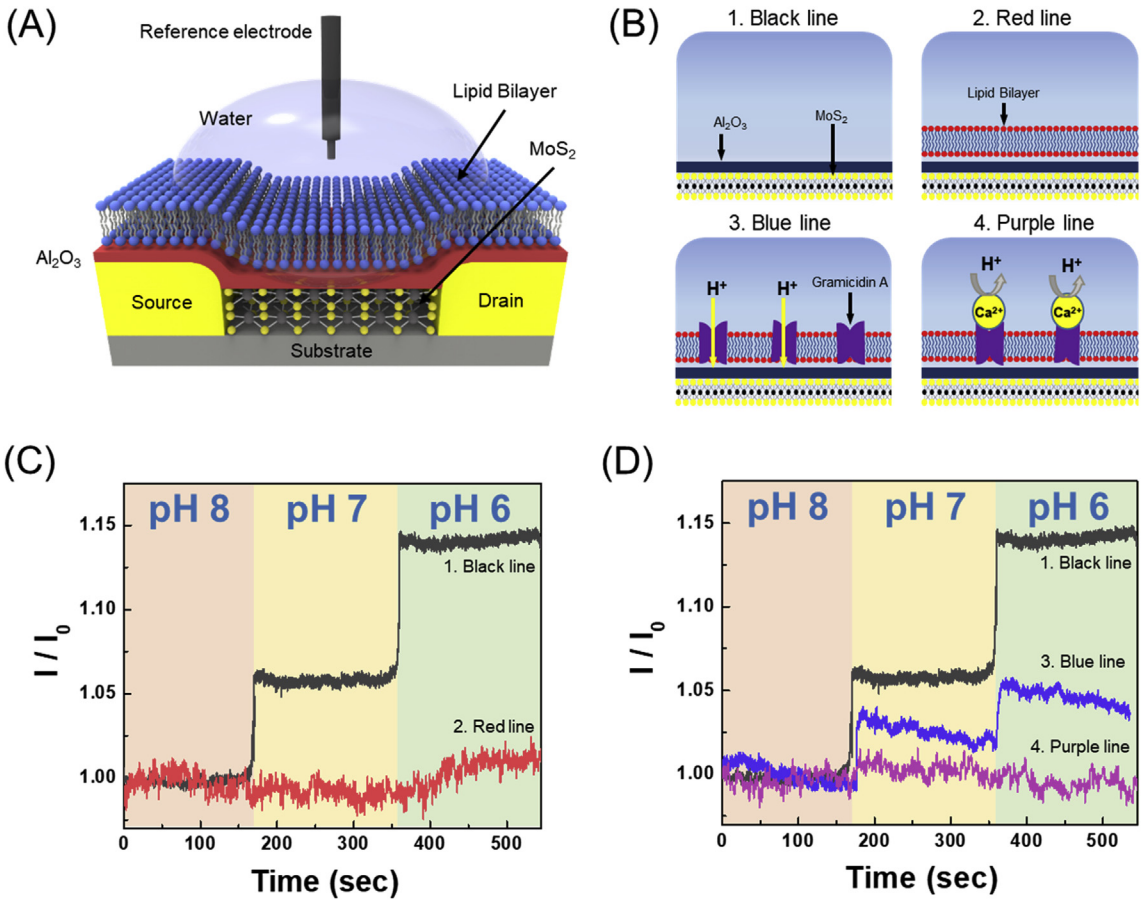

Fig. 6. Schematic of the device and pH response of the device with the lipid bilayer and gramicidin A. (A) Schematic of the MoS_2 FET device after Al_2O_3 deposition for bioelectronics. (B) Schematic of the device measurement environment in a pH buffer solution. (C) Real-time measurement of the uncoated device (black line) and lipid-coated device (red line) in pH 6, 7, and 8 solutions. (D) Real-time measurement of the bare device (black line), the device after incorporation of gramicidin A (blue line), and the device with the passage of the protein blocked by calcium ions (purple line) in the pH buffer solution. (For interpretation of the references to color in this figure legend, the reader is referred to the Web version of this article.)

for small monovalent cations to passively transport within the biological system, as shown in Fig. 6B (blue line). Thus, the MoS_2 device was affected by protons transported through the ion channel in the SLB, which caused a slight current increase in the device with a lower-pH solution, as observed in Fig. 6D (blue line). The device was fully covered with the SLB. Thus, the drain–source current was low: approximately 10–20% of that of the bare device. The ion channels of gramicidin A were blocked by calcium ions (Ca^{2+}) binding at the entrance of the transmembrane peptide pores, as shown in Fig. 6B (purple line). The addition of 1 mM of Ca^{2+} ions to the PDMS reservoir caused the current to change such that the purple line was constant irrespective of pH (Fig. 6D, purple line). The platform detected the pH change in real time, and the detection could be controlled by the proton channel and Ca^{2+} ion. In the measurements, bionanoelectronic devices could detect proton signals and selectively convert them to electronic signals via passive transport of gramicidin A.

4. Conclusion

In summary, we developed the large-scale synthesis of two-dimensional MoS_2 via CVD process and the fabrication of a stable liquid-gated MoS_2 field effect transistor. Although the electronic properties and stability of the 2D transition-metal dichalcogenides superior in air ambient is questionable in wet environment, our experiment results show that for lipid bilayer coating incorporating biomolecules, the hydrophobic nature of MoS_2 surface can be tuned by atomic layer deposition of Al_2O_3 or plasma treatment, and it makes MoS_2 transistor a suitable candidate for nanoelectronic device architecture operating in an electrolyte environment. We demonstrated for the first time not only the formation of supported lipid bilayer on the semiconducting MoS_2, but also a proof-of-concept of a 2D bionanoelectronic device based on lipid/MoS_2 hybrid to monitor ion channel activity. Although lipid bilayer-MoS_2 device integrated with gramicidin A ion channel was used for our proof-of-concept study of a bionanoelectronics enabling signal transduction between biology and electronics, other 2D nanomaterials and various membrane proteins with sophisticated functionalities can be utilized for this platform. We believe that our proposed lipid bilayer-coated MoS_2 hybrid opens up potential utility of 2D nanomaterials for bioelectronic platform, but also would pave the way for bioelectronics, biosensors and cell monitoring applications.

Declarations of interest

None.

CRediT authorship contribution statement

Yunjeong Park: Conceptualization, Data curation, Formal analysis, Investigation, Writing - original draft, Validation. **Byunggil Kang:** Data curation, Formal analysis, Writing - original draft. **Cheol Hyoun Ahn:** Formal analysis. **Hyung Koun Cho:** Formal analysis. **Hyukjoon Kwon:** Data curation, Formal analysis. **Sungsu Park:** Formal analysis. **Junhwan Kwon:** Data curation, Formal analysis. **Myunghwan Choi:** Formal analysis. **Changgu Lee:** Resources, Writing - review & editing.

Kyunghoon Kim: Conceptualization, Formal analysis, Funding acquisition, Project administration, Resources, Supervision, Writing - review & editing.

Acknowledgements

This research was supported by the Basic Science Research Program through the National Research Foundation of Korea (NRF) funded by the Ministry of Science, ICT & Future Planning (NRF-2017R1C1B2011750 and 2016K1A1A2912707). This work was also supported by an NRF grant funded by the Korean Government (NRF-2018-Fostering Core Leaders of the Future Basic Science Program/ Global Ph.D. Fellowship Program) (No. NRF-2018H1A2A1062418).

Appendix A. Supplementary data

Supplementary data to this article can be found online at https://doi.org/10.1016/j.bios.2019.111512.

References

Albert, B., Johnson, A., Lewis, J., Raff, M., Robert, K., Walter, P., 2007. Molecular Biology of the Cell. Garland Science, New York.

Ang, P.K., Jaiswal, M., Lim, C.H.Y.X., Wang, Y., Sankaran, J., Li, A., Lim, C.T., Wohland, T., Barbaros, O., Loh, K.P., 2010. A bioelectronic platform using a graphene-lipid bilayer interface. ACS Nano 4 (12), 7387–7394.

Artyukhin, A.B., Shestakov, A., Harper, J., Bakajin, O., Stroeve, P., Noy, A., 2005. Functional one-dimensional lipid bilayers on carbon nanotube templates. J. Am. Chem. Soc. 127 (20), 7538–7542.

Chen, X., Zhang, H., Tunuguntla, R.H., Noy, A., 2019. Silicon nanoribbon pH sensors protected by a barrier membrane with carbon nanotube porins. Nano Lett. 19 (2), 629–634.

Chow, P.K., Singh, E., Viana, B.C., Gao, J., Luo, J., Li, J., Lin, Z., Elias, A.L., Shi, Y., Wang, Z., Terrones, M., Koratkar, N., 2015. Wetting of mono and few-layered WS_2 and MoS_2 films supported on Si/SiO_2 substrates. ACS Nano 9 (3), 3023–3031.

Dalila, R.,N., Md Arshad, M.K., Gopinath, S.C.B., Norhaimi, W.M.W., Fathil, M.F.M., 2019. Current and future envision on developing biosensor aided by 2D molybdenum disulfide (MoS_2) productions. Biosens. Bioelectron. 132 (1), 248–264.

Dumcenco, D., Ovchinnikov, D., Marinov, K., Lazic, P., Gibertini, M., Marzari, N., Sanchez, O.L., Kung, Y., Krasnozhon, D., Chen, M., Bertolazzi, S., Gillet, P., Morral, A.F., Radenovic, A., Kis, A., 2015. Large-area epitaxial monolayer MoS_2. ACS Nano 9 (4), 4611–4620.

Go, J., Nair, P.R., Alam, M.A., 2012. Theory of signal and noise in double-gated nanoscale electronic pH sensors. J. Appl. Phys. 112 (3), 034516.

Islam, M.R., Kang, N., Bhanu, U., Paudel, H.P., Erementchouk, M., Tetard, L., Leuenberger, M.N., Khondaker, S.I., 2014. Tuning the electrical property via defect engineering of single layer MoS_2 by oxygen plasma. Nanoscale 6 (17), 10033–10039.

Jiang, K., Nie, D., Huang, Q., Fan, K., Tang, Z., Wu, Y., Han, Z., 2019. Thin-layer MoS_2 and thionin composite-based electrochemical sensing platform for rapid and sensitive detection of zearalenone in human biofluids. Biosens. Bioelectron. 130, 322–329.

Kang, M., Day, C.A., Kenworthy, A.K., DiBenedetto, E., 2012. Simplified equation to extract diffusion coefficients from confocal FRAP data. Traffic 13 (12), 1589–1600.

Kang, M.C., Andreani, M., Kenworthy, A.K., 2015. Validation of normalizations, scaling, and photofading corrections for FRAP data analysis. PLoS One 10 (5), e0127966.

Kaushik, S., Tiwari, U.K., Pal, S.S., Sinha, R.K., 2019. Rapid detection of Escherichia coli using fiber optic surface plasmon resonance immunosensor based on biofunctionalized Molybdenum disulfide (MoS_2) nanosheets. Biosens. Bioelectron. 126, 501–509.

Kim, K., Park, C., Kwon, D., Kim, D., Meyyappan, M., Jeon, S., Lee, J.S., 2016. Silicon nanowire biosensors for detection of cardiac troponin I (cTnI) with high sensitivity. Biosens. Bioelectron. 77, 695–701.

Kireev, D., Offenhausser, A., 2018. Graphene & two-dimensional devices for bioelectronics and neuroprosthetics. 2D Mater. 5 (4), 042004.

Lee, D.W., Lee, J., Sohn, I.Y., Kim, B.Y., Son, Y.M., Bark, H., Jung, J., Choi, M., Kim, T.H., Lee, C., Lee, N.E., 2015. Field-effect transistor with a chemically synthesized MoS_2 sensing channel for label-free and highly sensitive electrical detection of DNA hybridization. Nano Res. 8 (7), 2340–2350.

Lee, Y.H., Zhang, X.Q., Zhang, W., Chang, M.T., Lin, C.T., Chang, K.D., Yu, Y.C., Wang, J.T.W., Chang, C.S., Li, L.J., Lin, T.W., 2012. Synthesis of large-area MoS_2 atomic layers with chemical vapor deposition. Adv. Mater. 24 (17), 2320–2325.

Li, H., Zhang, Q., Yap, C.C.R., Tay, B.K., Edwin, T.H.T., Olivier, A., Baillargeat, D., 2012. From bulk to monolayer MoS_2: evolution of Raman scattering. Adv. Funct. Mater. 22 (7), 1385–1390.

Mao, S., Chang, J.B., Pu, H.H., Lu, G.H., He, Q.Y., Zhang, H., Chen, J.H., 2017. Two-dimensional nanomaterial-based field-effect transistors for chemical and biological sensing. Chem. Soc. Rev. 46 (22), 6872–6904.

Misra, N., Martinez, J.A., Huang, S.C.J., Wang, Y.M., Stroeve, P., Grigoropoulos, C.P., Noy, A., 2009. Bioelectronic silicon nanowire devices using functional membrane proteins. Proc. Natl. Acad. Sci. U. S. A. 106 (33), 13780–13784.

Noy, A., 2011. Bionanoelectronics. Adv. Mater. 23 (7), 807–820.

Qiao, X., Li, K., Xu, J., Cheng, N., Sheng, Q., Cao, W., Yue, T., Zheng, J., 2018. Novel electrochemical sensing plaform for ultrasensitive detection of cardiac troponin I based on aptamer-MoS_2 nanoconjugate. Biosens. Bioelectron. 113, 142–147.

Sarkar, D., Liu, W., Xie, X.J., Anselmo, A.C., Mitragotri, S., Banerjee, K., 2014. MoS_2 field-effect transistor for next-generation label-free biosensors. ACS Nano 8 (4), 3992–4003.

Tunuguntla, R.H., Bangar, M.A., Kim, K., Stroeve, P., Grigoropoulos, C., Ajo-Franklin, C.M., Noy, A., 2015. Bioelectronic light-gated transistors with biologically tunable performance. Adv. Mater. 27 (5), 831–836.

Yin, Z.Z., Cheng, S.W., Xu, L.B., Liu, H.Y., Huang, K., Li, L., Zhai, Y.Y., Zheng, Y.B., Liu, H.Q., Shao, Y., Zhang, Z.L., Lu, Y.X., 2018. Highly sensitive and selective sensor for sunset yellow on moleculary imprinted polydopamine-coated multi-walled carbon nanotubes. Biosens. Bioelectron. 100, 565–570.

Zhao, Z.Y., Dai, W.W., 2015. Electronic structure and optical properties of BiOl ultrathin films for photocatalytic water splitting. Inorg. Chem. 54 (22), 10732–10737.

Zhang, Q., Xiao, X., Zhao, R., Lv, D., Xu, G., Lu, Z., Sun, L., Lin, S., Gao, X., Zhou, J., Jin, C., Ding, F., Jiao, L., 2015. Two-dimensional layered heterostructures synthesized from core-shell nanowires. Angew Chem. Int. Ed. Engl. 54 (31), 8957–8960.

Zhang, T., Liu, J., Wang, C., Leng, X., Xiao, Y., Fu, L., 2017. Synthesis of graphene and related two-dimensional materials for bioelectronics devices. Biosens. Bioelectron. 89 (1), 28–42.